Int J Adv Manuf Technol (2017) 92:2939–2952
DOI 10.1007/s00170-017-0265-6

ORIGINAL ARTICLE

Modeling and optimization of the flute profile of micro-drill

Suyan Zhang[1] · **Xibin Wang**[1] · **Zhiqiang Liang**[1] · **Tianfeng Zhou**[1] · **Li Jiao**[1] · **Pei Yan**[1]

Received: 13 November 2016 / Accepted: 6 March 2017 / Published online: 13 April 2017
© Springer-Verlag London 2017

Abstract The profile of drill flute has a great influence on the drilling performance of micro-drill. It is promising to obtain a desired flute profile with a standard wheel by adjusting the wheel position parameters during the grinding process. To investigate the flute profile characteristics under different wheel position parameters and its effect on the drilling performance, this paper presents a method for modeling and optimization of the micro-drill flute considering the wheel installation angle and the offset distance from the wheel origin to the drill blank origin. Based on this model, the flute profile of micro-drill is numerically simulated by MATLAB software firstly, and then, the 3D model of micro-drill with different flute profiles is established by UG software. Finally, the micro-drilling process on 304 austenitic stainless steel is simulated by DEFORM software, and the chip morphology and the drilling force are analyzed and discussed. The results show that the wheel installation angle has an obvious effect on the flute profile and its radial rake angle and flute width, and the wheel offset distance only influences the flute width evidently. The micro-drill with flute ground by smaller wheel installation angle owns straighter cutting lip shape and larger chip evacuation capacity, and its thrust force and torque are smaller than those of other micro-drills. Moreover, spiral chip is generated due to the intense side curl and up curl of the chip, resulting in the easiness of the chip removal. However, for the micro-drills with flute ground by larger wheel installation angle, the chip morphology is string and the drilling force is larger. At last, the mathematical model of the drill flute and its numerical simulation result are validated by experimentally fabricating the micro-drill flute. Then, the optimized micro-drill is manufactured by a six-axis computer numerical control (CNC) grinding machine, and its flute profile is fabricated using a standard conical grinding wheel with a smaller wheel installation angle.

Keywords Flute profile · Micro-drill · Wheel position parameters · Drilling performance

✉ Zhiqiang Liang
liangzhiqiang@bit.edu.cn

Suyan Zhang
zsyangela@sina.com

Xibin Wang
cutting0@bit.edu.cn

Tianfeng Zhou
zhoutf@bit.edu.cn

Li Jiao
jiaoli@bit.edu.cn

Pei Yan
pyan@bit.edu.cn

[1] Key Laboratory of Fundamental Science for Advanced Machining, Beijing Institute of Technology, Beijing 100081, China

1 Introduction

The helical flute, as an essential component of micro-drill, has a great influence on the drilling performance. It defines the cutting lip and rake angle, provides the space for chip evacuation, and influences the strength and stability of the drill [1, 2]. The design and optimization of drill flute profile are closely bound up with the grinding process. During the flute grinding process, the helical flute is generated by the relative helical motion of the wheel and cylindrical blank, and the grinding parameters including the wheel profile and wheel position determine the flute profile and its performance [3].

Over the past decades, many researches have been focused on the modeling and machining of the drill flutes, and they can

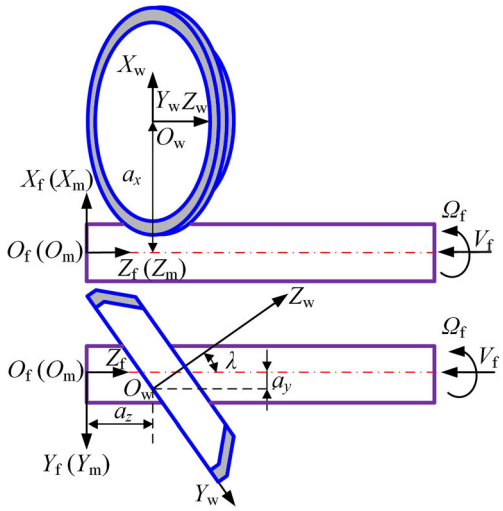

Fig. 1 Schematic illustration of the flute grinding operation

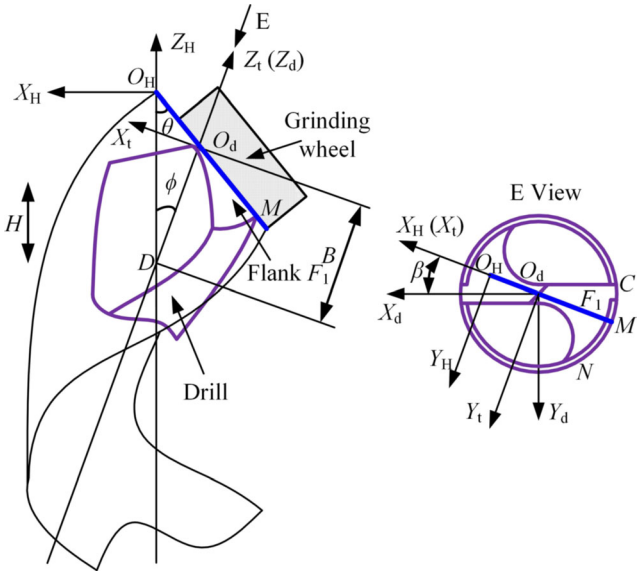

Fig. 3 The mathematical model of the flank surface of helical drill point

be divided into two methods: the direct and the indirect methods. The indirect method is to determine the wheel profile based on the wheel position and the desired flute profile [4–7]. However, the calculated wheel shapes are often complicated and not practical in industry. On the other hand, the direct method is to calculate the cross-sectional profile of the helical flute according to the given wheel profile and its position during the grinding process. Considering the wheel as a series of thin disks, the flute profile is developed as the envelope of the superimposed cutting paths of the individual disks [8, 9]. With this approach, Zhang et al. [10] proposed a practical modeling method of drill flute with a standard straight wheel. A desired flute profile can be generated by a standard wheel with a proper wheel position. Therefore, some researches have been carried out to obtain the wheel position parameters on the basis of the flute and wheel profile. Karpuschewski [11] presented an algorithm for the automatic search of the wheel position in flute grinding. By calculating the wheel position, Tang et al. [12] proposed a grinding method of the drill with a desired rake angle and core radius. Ren et al. [13] presented a novel five-axis grinding method of flute using standard 1V1/1A1 wheels to ensure the accuracy of the desired rake angle, core radius, and flute width. Beju et al. [14] presented a method for generating desired drill flute with conical grinding wheel and verified the validity of the presented method by grinding experiment.

Furthermore, some researchers investigated the effect of flute profile on the drilling or milling performance. By adjusting the wheel position parameters, Kim et al. [15] designed and manufactured a series of end mill flutes with different rake angles and clearance angles and analyzed the corresponding milling performance to obtain the optimal flute profile. Xiao et al. [16] investigated the influence of wheel geometry and positional parameters on the flute profile and found that the wheel setup angle and radius shape have a significant impact on the rake angle and flute width.

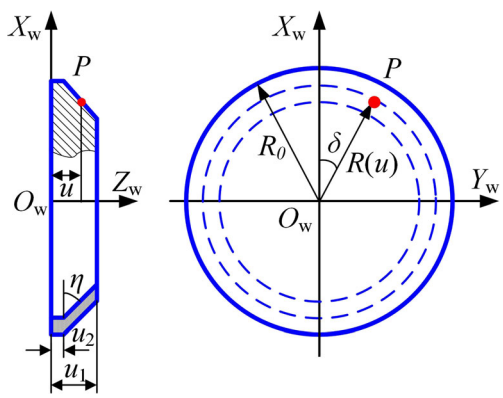

Fig. 2 Illustration of grinding wheel geometry

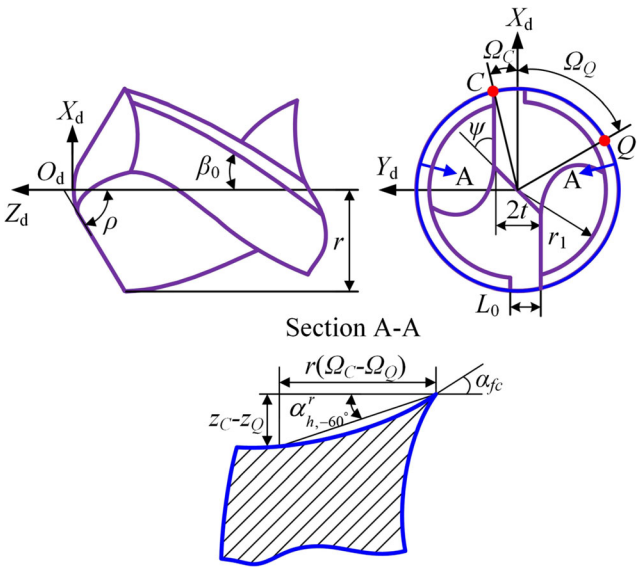

Fig. 4 The schematic diagram of the geometric parameters of micro-drills

Table 1 The geometric parameters of the micro-drill

Geometric parameters	Drill radius r (mm)	Web thickness $2t$ (mm)	Helical angle of the flute β_0 β(°)	Clearance radius r_1 (mm)	Margin width L_0 (mm)
Value	0.25	0.125	30	0.2125	0.075
Geometric parameters	Semi-point angle ρ (°)	Chisel edge angle ψ (°)	Lip clearance angle α_{fc} (°)	Heel clearance angle (°)	
Value	59	55	12	15	

However, the current researches on the design and optimization of the flute profile mainly focus on the majorization of the radial rake angle and flute width. But the optimization objects (the radial rake angle and flute width) cannot directly and effectively reflect the drilling performance. Therefore, the effect of the geometry characteristics of micro-drills with different flute profiles on the drilling performance should be analyzed and discussed, and a desired drill flute should be given by comprehensive evaluation on the micro-drilling performance.

In this paper, a method for modeling and optimization of the micro-drill flute is presented. Firstly, considering the wheel installation angle and the offset distance from the wheel origin to the drill blank origin, the flute profile of micro-drill is simulated by MATLAB software and the effect of wheel position parameters on the radial rake angle and flute width is investigated. Then, based on the numerical results, the 3D model of micro-drill with different flute profiles is established by UG software. Finally, a finite element model is generated by DEFORM software to simulate the micro-drilling process on 304 austenitic stainless steel, and the chip morphology and drilling force are analyzed and discussed to determine the optimal flute profile.

2 Mathematical model of the micro-drill

2.1 Mathematical model of the grinding drill flute

In the drill flute grinding process, the relative helical motion of the wheel and the cylindrical blank generates the helical flute. Figure 1 shows the schematic illustration of the flute grinding operation. The cylindrical blank rotates and moves along its own axis at a speed Ω_f and V_f enabling the formation of the helical flute. The coordinate system $O_wX_wY_wZ_w$ is established on the grinding wheel; the origin O_w is at the center of the larger lateral face; Z_w-axis is coinciding with the wheel axis; X_w and Y_w axes are on the lateral face and perpendicular to each other. The coordinate system $O_fX_fY_fZ_f$ is attached to the initial position of the cylindrical blank; Z_f-axis is along with the blank axis, and X_f-axis is parallel with X_w-axis. The coordinate system $O_mX_mY_mZ_m$ is established on the cylindrical blank, and it is dynamically changed with the helical motion of the cylindrical blank. Therefore, the wheel position in the blank coordinate system can be determined by the coordinates (a_x, a_y, a_z) of point O_w and the angle λ between O_wZ_w and O_fZ_f (namely the wheel installation angle).

The geometry of the grinding wheel is illustrated in Fig. 2, and it is defined with four parameters; the wheel radius R_0, the wheel thickness u_1, the conical angle η, and the width u_2. In the wheel coordinate system, the coordinate of an arbitrary point P on the wheel surface can be derived as

$$\begin{aligned}\boldsymbol{R}_{\mathbf{w}}(u,\delta) &= [X_{\mathrm{Pw}},\ Y_{\mathrm{Pw}},\ Z_{\mathrm{Pw}}]^{\mathrm{T}} \\ &= [R(u)\cos\delta,\ R(u)\sin\delta,\ u]^{\mathrm{T}}\end{aligned} \tag{1}$$

where $R(u) = \begin{cases} R_0 & 0 \le u \le u_2 \\ R_0 - (u-u_2)\cot\eta & u_2 < u \le u_1 \end{cases}$ and u and δ are the parameters of point P on the wheel surface.

In this study, the modeling approach is based on the direct method. Assuming that the wheel is composed of finite thin disks, the disks generate different cutting paths; then, the flute profile is formed by the envelope of the superimposed cutting paths.

After rotating $O_wX_wY_wZ_w$ coordinate system around X_w-axis by angle λ and translating O_w to O_f by coordinate (a_x, a_y, a_z), the coordinate frame $O_fX_fY_fZ_f$ is attained. Therefore, the transformation matrix between $O_wX_wY_wZ_w$ system and $O_fX_fY_fZ_f$ system is

$$\begin{aligned}\boldsymbol{R}_{\mathbf{f}} &= \mathrm{Rot}(X_{\mathrm{w}},-\lambda)\cdot\ \boldsymbol{R}_{\mathbf{w}} + \mathrm{Trans}\left(a_x,\ a_y, a_z\right) \\ &= \begin{bmatrix} 1 & 0 & 0 \\ 0 & \cos\lambda & -\sin\lambda \\ 0 & \sin\lambda & \cos\lambda \end{bmatrix} \cdot \boldsymbol{R}_{\mathbf{w}} + \begin{bmatrix} a_x \\ a_y \\ a_z \end{bmatrix}\end{aligned} \tag{2}$$

Table 2 The wheel profile and position parameters

Parameters	Installation angle λ (°)	Distance a_x (mm)	Distance a_y (mm)	Distance a_z (mm)
Value	40-60	67.5625	0-21	0
Parameters	Wheel radius R_0 (mm)	Wheel thickness u_1 (mm)	Wheel thickness u_2 (mm)	Wheel conical angle η (°)
Value	67.5	4	0	45

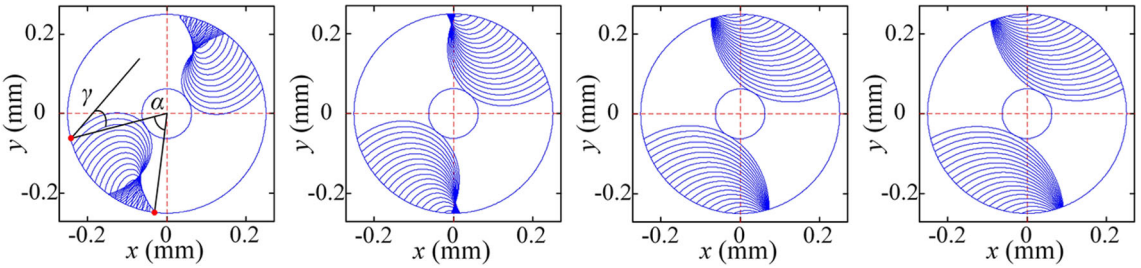

(a) λ=60° (b) λ=50° (c) λ=42.22° (d) λ=40°

Fig. 5 Influence of wheel installation angle λ on cross-sectional profile of drill flute with a_x = 67.5625 mm, a_y = 0. **a** λ = 60°. **b** λ = 50°. **c** λ = 42.22°. **d** λ = 40°

Substituting Eq. (1) into Eq. (2), the coordinate of point P in $O_fX_fY_fZ_f$ system is derived as

$$\boldsymbol{R}_{\mathbf{f}}(u,\delta)=\begin{bmatrix}X_{\mathrm{Pf}}\\Y_{\mathrm{Pf}}\\Z_{\mathrm{Pf}}\end{bmatrix}=\begin{bmatrix}R(u)\cos\delta+a_x\\R(u)\sin\delta\cos\lambda-u\sin\lambda+a_y\\R(u)\sin\delta\sin\lambda+u\cos\lambda+a_z\end{bmatrix} \quad (3)$$

According to the flute grinding operation, assuming that the blank rotates at a certain angle φ around O_fZ_f-axis and moves by a specified distance $r\varphi/\tan(\beta_0)$ along O_fZ_f-axis, where r is the drill radius, β_0 is the helical angle of the drill flute. So, the coordinate of point P in the coordinate system $O_mX_mY_mZ_m$ can be expressed as

$$\boldsymbol{R}_{\mathbf{m}}(u,\delta,\varphi)=\begin{bmatrix}X_{\mathrm{Pm}}\\Y_{\mathrm{Pm}}\\Z_{\mathrm{Pm}}\end{bmatrix}=\begin{bmatrix}X_{\mathrm{Pf}}\cos\varphi-Y_{\mathrm{Pf}}\sin\varphi\\X_{\mathrm{Pf}}\sin\varphi+Y_{\mathrm{Pf}}\cos\varphi\\Z_{\mathrm{Pf}}+r\varphi\big/\tan(\beta_0)\end{bmatrix} \quad (4)$$

Assuming that Z_{Pm} = 0, the angle φ can be derived as $\varphi = -Z_{Pf}\tan(\beta_0)/r$, so the coordinate of point P in the transverse plane Z_{Pm} = 0 can be derived as

$$\begin{aligned}\boldsymbol{R}_{\mathrm{m}}(u,\delta)&=\begin{bmatrix}X_{\mathrm{Pm}}(u,\delta)\\Y_{\mathrm{Pm}}(u,\delta)\end{bmatrix}\\&=\begin{bmatrix}X_{\mathrm{Pf}}\cos\left(-Z_{\mathrm{Pf}}\tan(\beta_0)\big/r\right)-Y_{\mathrm{Pf}}\sin\left(-Z_{\mathrm{Pf}}\tan(\beta_0)\big/r\right)\\X_{\mathrm{Pf}}\sin\left(-Z_{\mathrm{Pf}}\tan(\beta_0)\big/r\right)+Y_{\mathrm{Pf}}\cos\left(-Z_{\mathrm{Pf}}\tan(\beta_0)\big/r\right)\end{bmatrix}\end{aligned} \quad (5)$$

In addition, the point should be enclosed in the circular area of the drill cross section, so X_{Pm} and Y_{Pm} coordinates are valid if $(X_{Pm}^2 + Y_{Pm}^2) \le r$. Then, the cutting path of one thin disk is generated with constant u and variable δ. So, the flute cross-sectional profile can be obtained by the envelope of the cutting paths generated with different parameters u and δ.

In order to describe the enveloped curve numerically, the envelope condition is given by [10]

$$\frac{\partial X_{\mathrm{Pm}}}{\partial\delta}\times\frac{\partial Y_{\mathrm{Pm}}}{\partial u}-\frac{\partial Y_{\mathrm{Pm}}}{\partial\delta}\times\frac{\partial X_{\mathrm{Pm}}}{\partial u}=0 \quad (6)$$

Substituting Eq. (4) into Eq. (6), the envelop equation is derived as

$$\begin{aligned}&\frac{r}{\tan(\beta_0)}\left(\frac{\partial X_{\mathrm{Pf}}}{\partial\delta}\frac{\partial Y_{\mathrm{Pf}}}{\partial u}-\frac{\partial Y_{\mathrm{Pf}}}{\partial\delta}\frac{\partial X_{\mathrm{Pf}}}{\partial u}\right)+Y_{\mathrm{Pf}}\left(\frac{\partial Z_{\mathrm{Pf}}}{\partial\delta}\frac{\partial Y_{\mathrm{Pf}}}{\partial u}-\frac{\partial Y_{\mathrm{Pf}}}{\partial\delta}\frac{\partial Z_{\mathrm{Pf}}}{\partial u}\right)\\&\quad+X_{\mathrm{Pf}}\left(\frac{\partial Z_{\mathrm{Pf}}}{\partial\delta}\frac{\partial X_{\mathrm{Pf}}}{\partial u}-\frac{\partial X_{\mathrm{Pf}}}{\partial\delta}\frac{\partial Z_{\mathrm{Pf}}}{\partial u}\right)=0\end{aligned} \quad (7)$$

Then, the coordinates of points on the non-enveloped curve can be obtained by Eq. (5) with u = 0. By substituting different u, the corresponding envelop angle δ is deduced via Eq. (7) and the coordinates of the points on enveloped curve are calculated by Eq. (5).

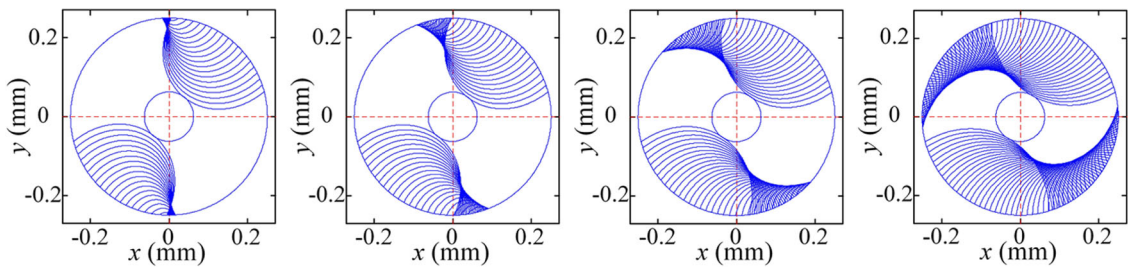

(a) a_y=0,a_x=67.5625mm (b) a_y=7mm,a_x=67.2960mm (c) a_y=14mm,a_x=66.4912mm (d) a_y=21mm,a_x=65.1272mm

Fig. 6 Influence of wheel offset distance a_y on cross-sectional profile of drill flute with parameter λ = 50°. **a** a_y = 0, a_x = 67.5625 mm. **b** a_y = 7 mm, a_x = 67.2960 mm. **c** a_y = 14 mm, a_x = 66.4912 mm. **d** a_y = 21 mm, a_x = 65.1272 mm

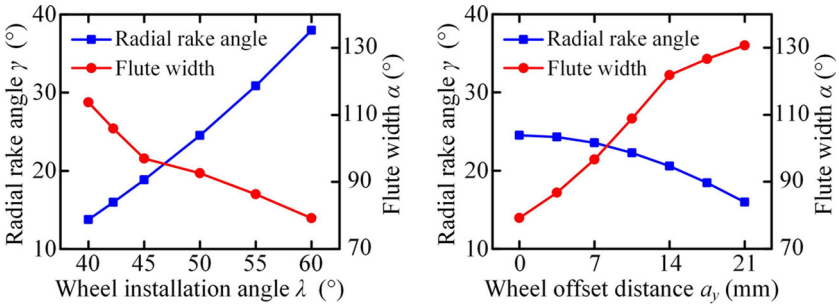

(a) Wheel installation angle λ (b) Wheel offset distance a_y

Fig. 7 The radial rake angle γ and flute width α versus wheel installation angle λ and wheel offset distance a_y. **a** Wheel installation angle λ. **b** Wheel offset distance a_y

In order to obtain the mathematical model of the drill flute in system $O_dX_dY_dZ_d$ ($X_dY_dZ_d$ is the coordinate frame built in the drill, with O_d locating at the drill tip, Z_d-axis coinciding with the drill axis), the coordinate points of the flute profile are processed by cubic-spline interpolation, and the equation of cross-sectional profile of drill flute is expressed as $y_d = f_H(x_d)$. The flute surface can be generated by the helical motion of the cross-sectional profile, so the parameter equation of drill flute is derived as

$$F_0: \begin{cases} X_d = w\cos v - f_H(w)\sin v \\ Y_d = w\sin v + f_H(w)\cos v \\ Z_d = rv/\tan\beta_0 \end{cases} \quad (8)$$

where w and v are variable parameters to generate the flute surface.

2.2 Mathematical model of the helical drill flank

Based on the mathematical model proposed by Zhang et al. [17], the mathematical model of helical drill flank is shown in Fig. 3. The flank F_1 is made by part of the helical surface generated by the helical motion of generatrix O_HM along Z_H-axis. $O_HX_HY_HZ_H$ is the coordinate frame of the helical surface. $O_dX_dY_dZ_d$ is the coordinate frame built in the drill. Rotating $O_dX_dY_dZ_d$ system around Z_d-axis by angle β, $O_tX_tY_tZ_t$ system is attained.

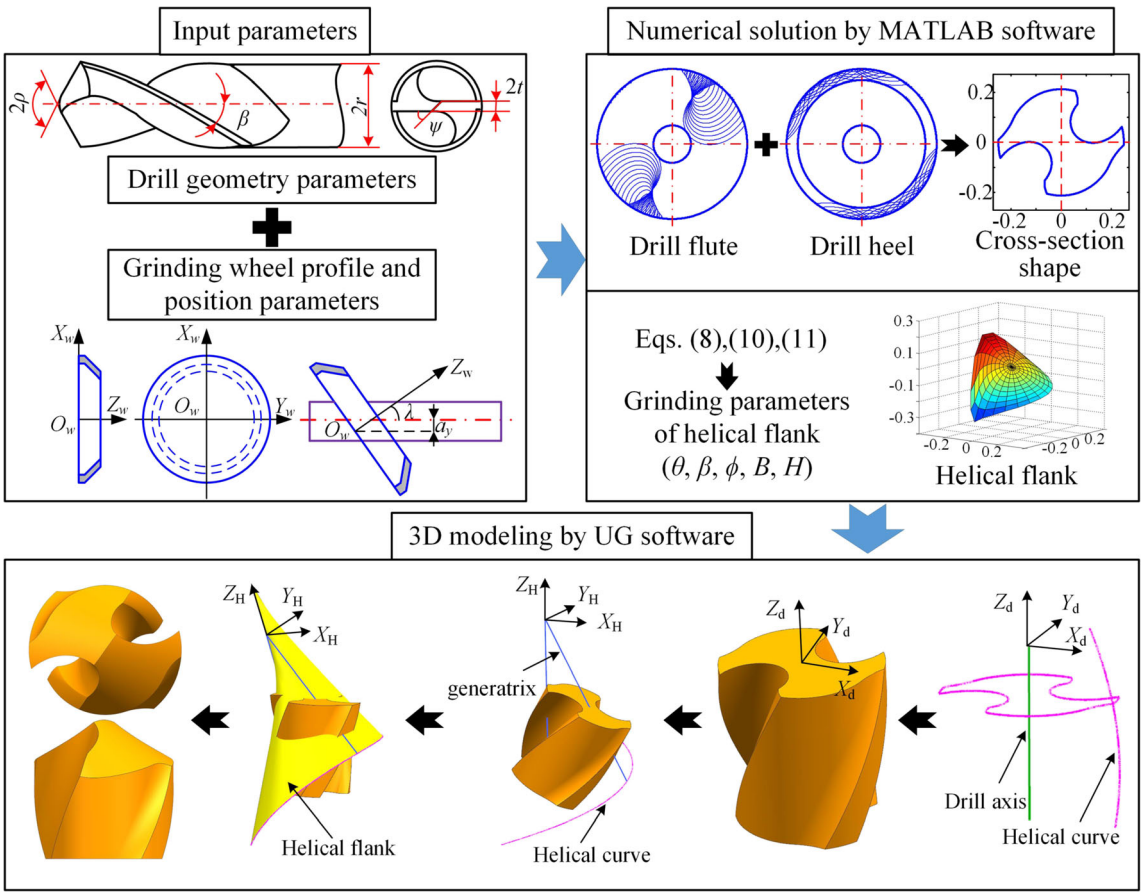

Fig. 8 Schematic diagram of micro-drill 3D modeling process

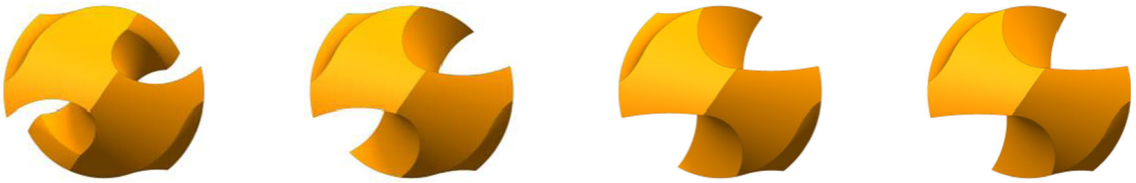

(a) Tool 1 λ=60°, a_y=0 (b) Tool 2 λ=50°, a_y=0 (c) Tool 3 λ=42.22°, a_y=0 (d) Tool 4 λ=40°, a_y=0

Fig. 9 Micro-drills with different flute profiles. **a** Tool 1 $\lambda = 60°$, $a_y = 0$. **b** Tool 2 $\lambda = 50°$, $a_y = 0$. **c** Tool 3 $\lambda = 42.22°$, $a_y = 0$. **d** Tool 4 $\lambda = 40°$, $a_y = 0$

Translating O_t to O_H by coordinate (x_0, y_0, z_0) and rotating $O_tX_tY_tZ_t$ system around Y_t-axis by angle ϕ, $O_HX_HY_HZ_H$ system is attained. Apart from ϕ and β, there are three other parameters for grinding the helical flank: θ, H, and B, where B is the distance between point O_d and D, H is the pitch of helical flank, and θ is the angle between wheel surface and Z_H-axis. The equation of the helical surface in $O_HX_HY_HZ_H$ system can be expressed as

$$F_1 : Z_H + \frac{\sqrt{X_H^2 + Y_H^2}}{\tan\theta} + \frac{H}{2\pi}\sin^{-1}\left(\frac{Y_H}{\sqrt{X_H^2 + Y_H^2}}\right) = 0 \quad (9)$$

By coordinate transformation, the equation of helical flank in the system $X_dY_dZ_d$ can be expressed as

$$\begin{aligned} F_1 : {} & Z_d\cos\phi - B\frac{\sin\phi}{\tan\theta} + \sin\phi(X_d\cos\beta - Y_d\sin\beta) \\ & + \frac{\sqrt{[\cos\phi(X_d\cos\beta - Y_d\sin\beta) - \sin\phi(Z_d + B)]^2 + (Y_d\cos\beta + X_d\sin\beta)^2}}{\tan\theta} \\ & + \frac{H}{2\pi}\sin^{-1}\left(\frac{Y_d\cos\beta + X_d\sin\beta}{\sqrt{[\cos\phi(X_d\cos\beta - Y_d\sin\beta) - \sin\phi(Z_d + B)]^2 + (Y_d\cos\beta + X_d\sin\beta)^2}}\right) = 0 \end{aligned} \quad (10)$$

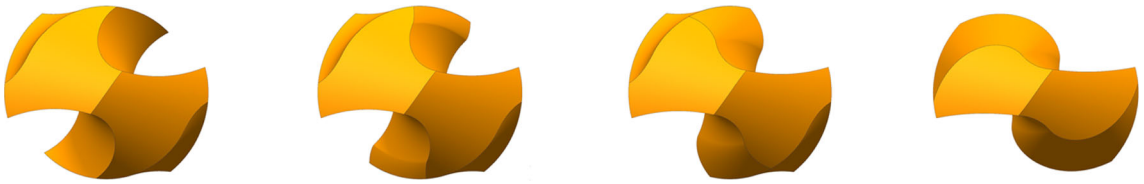

(a) Tool 5 λ=50°, a_y=0 (b) Tool 6 λ=50°, a_y=7mm (c) Tool 7 λ=50°, a_y=14mm (d) Tool 8 λ=50°, a_y=21mm

Fig. 10 Micro-drills with different flute profiles. **a** Tool 5 $\lambda = 50°$, $a_y = 0$. **b** Tool 6 $\lambda = 50°$, $a_y = 7$ mm. **c** Tool 7 $\lambda = 50°$, $a_y = 14$ mm. **d** Tool 8 $\lambda = 50°$, $a_y = 21$ mm

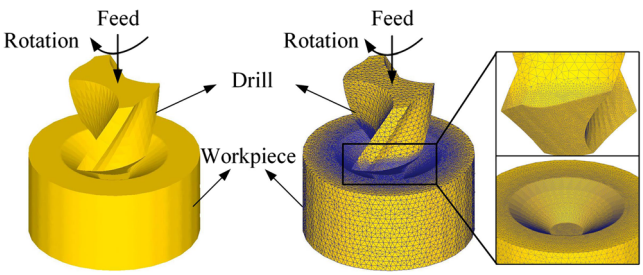

Fig. 11 The finite element model of micro-drilling

Table 3 The simulation parameters of the micro-drilling

Drilling parameters		Materials		Friction parameter		Separation
Rotation speed N	14,000 r/min	Drill	Carbide (15% cobalt)	Friction type	Shear	Cockcroft-Latham
Feed rate f	0.02 mm/r	Workpiece	AISI304	Friction value	0.7	

In addition, the relationship between drill geometry parameters and grinding parameters is [18]

$$\begin{cases} \rho = g_1(\theta,\ \beta,\ \phi,\ B,\ H) \\ \psi = g_2(\theta,\ \beta,\ \phi,\ B,\ H) \\ \alpha_{fc} = g_3(\theta,\ \beta,\ \phi,\ B,\ H) \\ \alpha^R_{h,-60^\circ} = g_4(\theta,\ \beta,\ \phi,\ B,\ H) \end{cases} \tag{11}$$

3 Numerical simulation and 3D modeling of the micro-drill

3.1 Numerical simulation of the flute profile of the micro-drill

In order to obtain the flute profile, a simulation program by MATLAB software is used to calculate the numerical solution. The geometric parameters of micro-drills are shown and listed in Fig. 4 and Table 1, and the section A-A is the cylindrical surface with the circle center O_d and the radius r [19]. The wheel profile and position parameters are listed in Table 2. The distance a_z has no effect on the flute profile due to the same cross-sectional shape along the drill axis, and the value of distance a_x ($a_x = R_0 + t$) is constant for the micro-drill flute with the same core radius. So in this study, the influence of wheel installation angle λ and offset distance a_y on the flute profile is analyzed and discussed.

The parameters listed in Tables 1 and 2 are substituted into the simulation program, and the cross-sectional profiles of micro-drill flutes are calculated. Figures 5 and 6 show the simulation results with different parameters λ and a_y. In addition, the radial rake angle γ and flute width α are used to evaluate the flute profile, as shown in Fig. 5a. The calculation method was presented by Ren et al. [13], and the calculation results are shown in Fig. 7.

It can be observed that the flute profile becomes conventional drill flute shape (Fig. 5c, d) with the decreased wheel installation angle λ, and the flute profile becomes parabolic flute shape (Fig. 6c, d) with the increased wheel offset distance a_y. Furthermore, Fig. 7 shows that the radial rake angle increases rapidly with the increased wheel installation angle λ and decreases slightly with the increased wheel offset distance a_y. With the decreased wheel installation angle λ and increased wheel offset distance a_y, the flute width of drill flute increases causing the reduction of micro-drill strength but improvement of the chip evacuation capacity. Thus, the wheel installation angle has an obvious effect on the flute profile and its radial rake angle and flute width, and the wheel offset distance only influences the flute width evidently but has little effect on the radial rake angle. Furthermore, although the radial rake angles of both conventional flute shown in Fig. 5c and parabolic flute shown in Fig. 6d are equal, their flute profiles are apparently different.

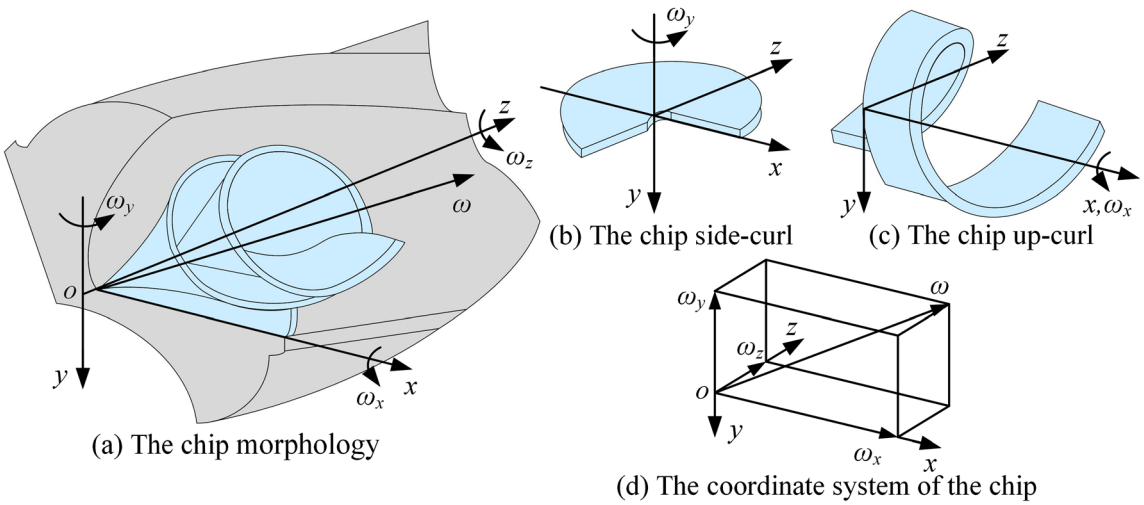

Fig. 12 The schematic diagram of the chip morphology

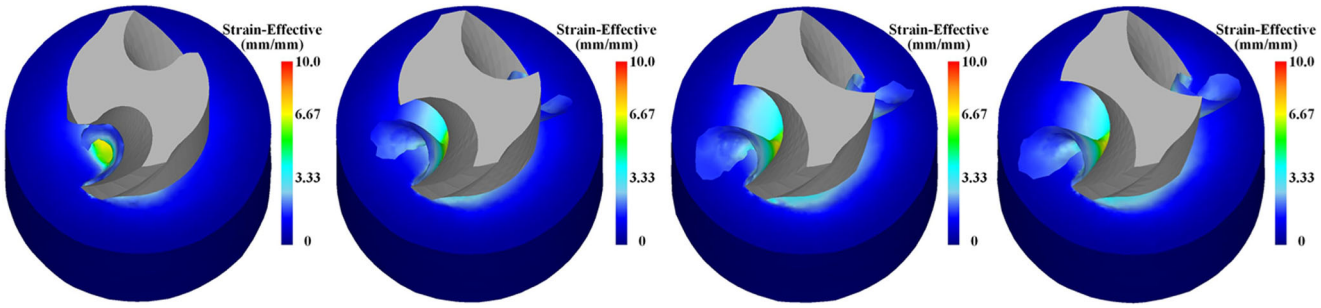

Fig. 13 Chip morphology of micro-drilling with tools 1, 2, 3, and 4 when drilling depth = 0.03 mm. **a** Tool 1 $\lambda = 60°$, $a_y = 0$. **b** Tool 2 $\lambda = 50°$, $a_y = 0$. **c** Tool 3 $\lambda = 42.22°$, $a_y = 0$. **d** Tool 4 $\lambda = 40°$, $a_y = 0$

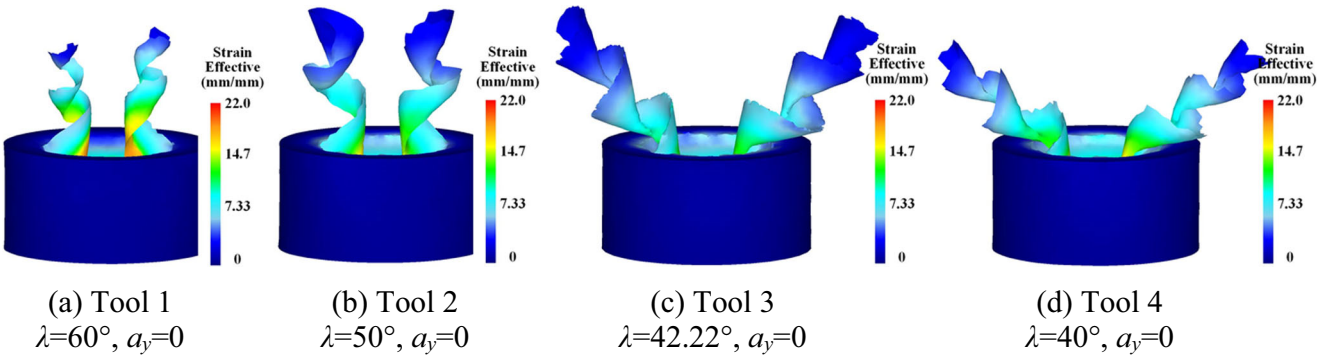

Fig. 14 Chip morphology of micro-drilling with tools 1, 2, 3, and 4 when drilling depth = 0.06 mm. **a** Tool 1 $\lambda = 60°$, $a_y = 0$. **b** Tool 2 $\lambda = 50°$, $a_y = 0$. **c** Tool 3 $\lambda = 42.22°$, $a_y = 0$. **d** Tool 4 $\lambda = 40°$, $a_y = 0$

3.2 3D modeling of the micro-drills with different flute profiles

The schematic diagram of micro-drill 3D modeling process is shown in Fig. 8. Substituting drill geometry parameters (r, t, β_0) listed in Table 1 and wheel profile and position parameters listed in Table 2 into Eqs. (5) and (7), the cross-sectional profile of drill flute is obtained. Similarly, taking geometry parameters (r, r_1, β_0) and wheel profile and position parameters into Eqs. (5) and (7), the cross-sectional profile of drill heel is obtained. In this research, the shape of drill heel is the same with constant wheel position parameters. Then, the numerical solution of cross-

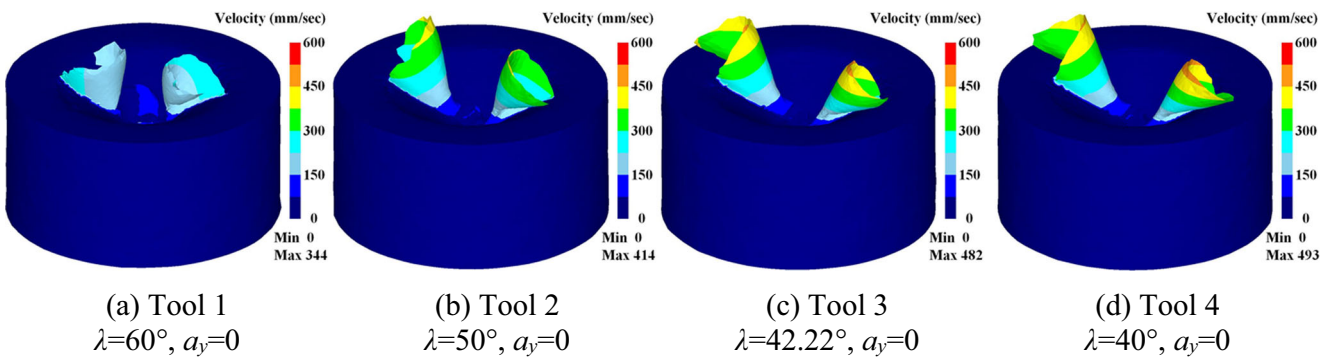

Fig. 15 Flow velocity of the chip along the cutting lip for different micro-drills when drilling depth = 0.03 mm. **a** Tool 1 $\lambda = 60°$, $a_y = 0$. **b** Tool 2 $\lambda = 50°$, $a_y = 0$. **c** Tool 3 $\lambda = 42.22°$, $a_y = 0$. **d** Tool 4 $\lambda = 40°$, $a_y = 0$

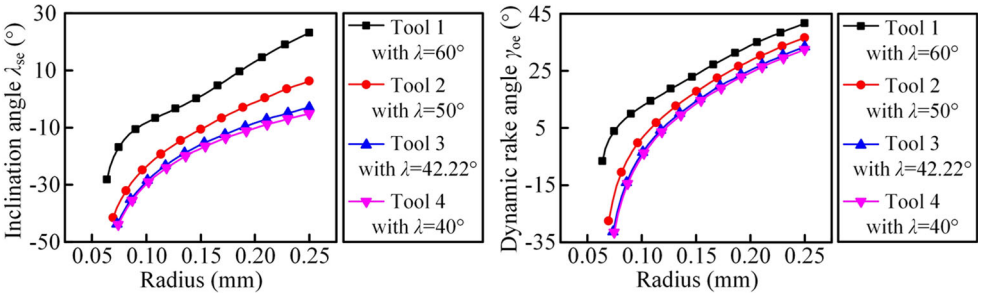

(a) The dynamic inclination angle (b) The dynamic rake angle

Fig. 16 Dynamic inclination angle and rake angle along cutting lip of tools 1, 2, 3, and 4 with f = 0.02 mm/r. **a** The dynamic inclination angle. **b** The dynamic rake angle

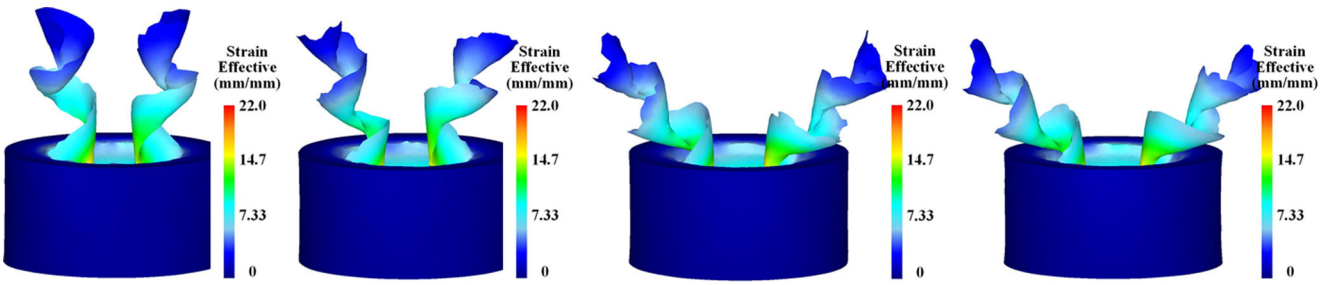

(a) Tool 5 λ=50°, a_y=0 (b) Tool 6 λ=50°, a_y=7mm (c) Tool 7 λ=50°, a_y=14mm (d) Tool 8 λ=50°, a_y=21mm

Fig. 17 Chip morphology of micro-drilling with tools 5, 6, 7, and 8 when drilling depth = 0.06 mm. **a** Tool 5 λ = 50°, a_y = 0. **b** Tool 6 λ = 50°, a_y = 7 mm. **c** Tool 7 λ = 50°, a_y = 14 mm. **d** Tool 8 λ = 50°, a_y = 21 mm

sectional shape of micro-drill is obtained by MATLAB software. According to the equations of helical flank and drill flute and the relationship listed in Eq. (11), the grinding parameters (θ, β, ϕ, B, H) of helical flank are calculated with the drill geometry parameters listed in Table 1.

Based on the numerical results solved by MATLAB software, the 3D model of micro-drills is established by UG software. Firstly, the points on the cross-sectional profile of drill flute are imported into the software, and the drill flute is generated by the sweep of cross-sectional profile along the drill axis and helical curve. Secondly, based on the grinding parameters of helical flank, the system $X_HY_HZ_H$ is built, and the helical flank is generated by the sweep of generatrix along Z_H-axis and helical curve. Lastly, the drill flute is pruned by helical flank, and the 3D model of micro-drill is established. The micro-drills with different flute profiles discussed in Sect. 2.1 are shown in Figs. 9 and 10.

4 Finite element simulation of the micro-drilling process

In order to compare the drilling performance of micro-drills with different flute profiles, the micro-drilling process is simulated by DEFORM software. The finite element model of micro-drilling is shown in Fig. 11. In order to reduce the simulation time, only drill point and a part of drill body are

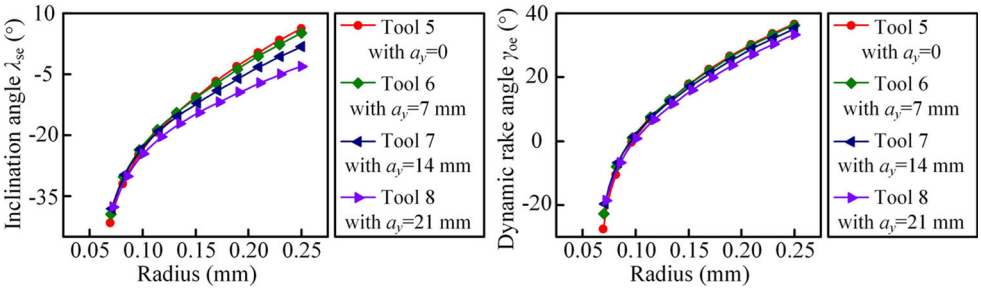

(a) The dynamic inclination angle (b) The dynamic rake angle

Fig. 18 Dynamic inclination angle and rake angle along cutting lip of tools 5, 6, 7, and 8 with f = 0.02 mm/r. **a** The dynamic inclination angle. **b** The dynamic rake angle

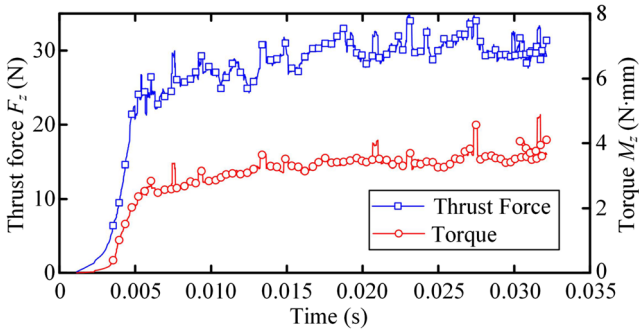

Fig. 19 The simulation result of drilling force by tool 1

set as the drill model, and a cylindrical workpiece with a conical concave surface is modeled as the workpiece. Local mesh refined method is used for the drill point due to its important role in the chip formation process. The drill movements including the feed and rotation are exerted on the drill axis, and all the freedoms of outside cylindrical surface are constrained. The micro-drilling parameters are listed in Table 3.

4.1 Chip morphology of the micro-drilling process

The drilling process is a complex oblique cutting process; workpiece material through plastic deformation tends to differ in chip morphology due to the different chip compression ratio. In general, the chip morphology is spiral. As shown in Fig. 12a, the coordinate system of the chip is defined as *oxyz* system, *x*-axis is coincident with the cutting lip, *z*-axis is along the drill axis, and *y*-axis is perpendicular to *x* and *z* axes. During the drilling process, the side curl phenomenon of the chip firstly occurs, because of the large change rate of the rake angle and cutting velocity along the cutting lip. The chip side curl phenomenon shown in Fig. 12b is that the chip rotates along *y*-axis and owns an angular velocity ω_y. As the drilling continues, due to the intense side curl, the chip is blocked by the drill web, and it is forced to up curl. The chip up curl phenomenon shown in Fig. 12c is that the chip rotates along the *x*-axis and owns an angular velocity ω_x. In addition, the chip rotates along the *z*-axis and owns an angular velocity ω_z due to the helical rake face. Finally, the rotation vector ω of the spiral chip is obtained by the composition of vectors ω_x, ω_y, and ω_z, as shown in Fig.12d.

When drilling depths are 0.03 and 0.06 mm, the simulation results of the chip morphology drilled by tools 1, 2, 3, and 4 are shown in Figs. 13 and 14. It can be seen that the side curl and up curl phenomena of the chip both occur, and they become more obvious from tool 1 to tool 4. In addition, the chip axis ω is gradually away from the drill axis from tool 1 to tool 4.

It should be noted that the chip side curl is related not only to the chip flow direction but also to the gradient of the chip flow velocity along the cutting lip (see Fig. 15), and the lip inclination angle λ_{se} and rake angle γ_{oe} are the main influence factors. The calculation equation of λ_{se} and γ_{oe} is expressed as [20]

$$\lambda_{se} = \sin^{-1}(\mathbf{b}\cdot\mathbf{r}), \gamma_{oe} = \tan^{-1}\left(\begin{vmatrix} g_x & g_y & g_z \\ r_x & r_y & r_z \\ o_x & o_y & o_z \end{vmatrix} \Big/ (\mathbf{g}\times\mathbf{o})\cdot(\mathbf{r}\times\mathbf{o})\right) \tag{12}$$

where **g** and **h** are the unit vectors normal to the rake and clearance surface, $\mathbf{g} = (g_x, g_y, g_z) = (\partial F_0/\partial x, \partial F_0/\partial y, \partial F_0/\partial z)$, $\mathbf{h} = (h_x, h_y, h_z) = (\partial F_1/\partial x, \partial F_1/\partial y, \partial F_1/\partial z)$. **b** is the unit vector along the cutting lip, $\mathbf{b} = (\mathbf{g}\times\mathbf{h}) / |\mathbf{g}\times\mathbf{h}|$. **r**, **s**, and **o** are the unit vectors normal to working reference plane, cutting edge plane, and orthogonal plane, $\mathbf{r} = \boldsymbol{V_e} / |\boldsymbol{V_e}|$, $\mathbf{s} = (\boldsymbol{V_e}\times\mathbf{b}) / |\boldsymbol{V_e}\times\mathbf{b}|$, $\mathbf{o} = \mathbf{s}\times\mathbf{r}$, and $\boldsymbol{V_e}$ is the resultant cutting velocity of any point (x, y, z) on the cutting lip, $\boldsymbol{V_e} = (-2\pi Ny, 2\pi Nx, Nf/1000)$ (N is the rotation speed; f is the feed rate).

The calculated result of the dynamic lip inclination angle λ_{se} and dynamic rake angle γ_{oe} is shown in Fig. 16. It can be seen that the lip inclination angle of Tool 4 with flute generated by smaller wheel installation angle is smaller than that of tools 1, 2, and 3, and this will make the chip flow toward the drill web direction other than the drill axis direction, so the side curl phenomenon of the chip drilled by tool 4 is most evident. In addition, the gradient of the chip flow velocity along the cutting lip, which will affect the chip side curl, is related not only to the cutting velocity but also to the chip compression ratio. The chip flow velocity can be calculated by the equation $v_{chip} = v_{cutting}/\Lambda_h$, where $v_{cutting}$ is the cutting velocity and Λ_h is the chip compression ratio. Moreover, the chip compression ratio Λ_h can be calculated using the equations $\Lambda_h = \cos(\phi - \gamma_{oe})/\sin\phi$ and $\phi = \pi/4 - (\beta_f - \gamma_{oe})$, where ϕ is the shear angle and β_f is the frictional angle. Thus, the rake angle has a great influence on the chip compression ratio. A larger rake angle offers a smaller chip compression ratio

Table 4 The drilling force of different micro-drills

Micro-drills	Thrust force (N)	Torque (N mm)	Micro-drills	Thrust force (N)	Torque (N mm)
Tool 1	30.2782	3.4125	Tool 5	10.5119	3.1041
Tool 2	10.5119	3.1041	Tool 6	9.8001	3.1840
Tool 3	7.4553	3.0400	Tool 7	8.6073	3.1455
Tool 4	7.2664	3.0149	Tool 8	7.4218	3.1011

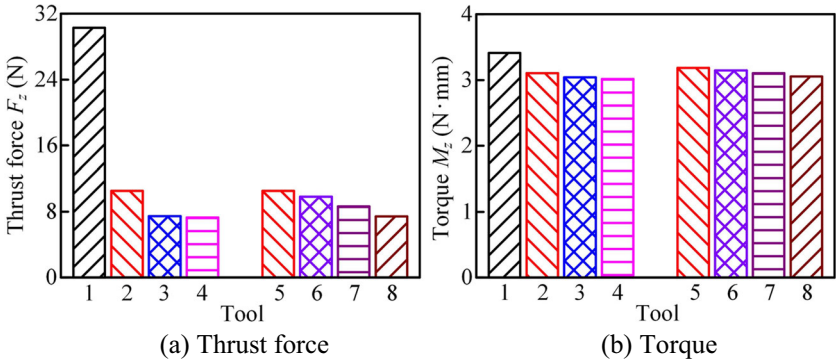

Fig. 20 The simulation results of drilling force by different micro-drills. **a** Thrust force. **b** Torque

resulting in a larger chip flow velocity. Figure 16b shows that the gradient of the rake angle along the cutting lip increases from tool 1 to 4, and this will enlarge the gradient of the chip flow velocity. As can be seen from Fig. 15, the gradient of the chip velocity along the cutting lip for tool 4 is larger than that of other tools, so the side curl of the chip cut by tool 4 is most significant. As the drilling continues, due to the intense side curl, the chip is blocked by the drill web, and it is forced to up curl. What is more, as the side curl of the chip is performed obviously, the chip is blocked by the drill web, resulting in the up curl tendency of the chip.

Therefore, not only the side curl phenomenon but also the up curl phenomenon of the chip drilled by tool 4 are the most obvious, i.e., the rotation vectors ω_x and ω_y of the chip drilled by tool 4 are both larger than that drilled by other micro-drills. The rotation vector ω_z is commensurate for tools 1, 2, 3, and 4, and the chip axis ω is composed by larger vectors ω_x and ω_y for tool 4, so the angle between the drill axis ω_z and the chip axis ω for tool 4 is larger than that for other micro-drills.

Consequently, during the drilling process with tools 1 and 2, the side curl and up curl of the chip are light, and the chip axis is close to the drill axis, so the chips slip a long distance along the rake face and string chips are generated which are easy to wrap around the drill. However, during the drilling process with tools 3 and 4, the slip distance of the chips along the rake face is smaller and spiral chips are generated resulting in the easiness of the chip removal and the reduction of the friction force between the chip and the drill.

When drilling depth is 0.06 mm, the simulation result of chip morphology drilled by tools 5, 6, 7, and 8 is shown in Fig. 17. The lip inclination angle and rake angle are shown in Fig. 18. It can be seen that the side curl and up curl phenomena of the chip are both obvious, and they enhance successively from tools 5 to 8. This is mainly caused by the increase of the negative value of the lip inclination angle from tools 5 to 8. However, the lip rake angle has little effect on the chip curl due to its inconspicuous change from tools 5 to 8. So, the angle between the chip axis and the drill axis increases due to the intense up curl and side curl of the chip. Finally, string chip is generated during the drilling process with tools 5 and 6, and spiral chips are generated during the drilling process with tools 7 and 8.

4.2 Drilling force by micro-drills with different flute profiles

The simulation result of drilling force by tool 1 is shown in Fig. 19. It is observed that the drilling force rapidly increases during the initial period and then becomes basically stable after the chisel edge and the cutting lip have completely drilled into the workpiece. Then, the average drilling force in stable phase is calculated, and the simulation results by different micro-drills are listed in Table 4 and shown in Fig. 20. It can be seen that the thrust force and torque decrease from tool 1 to tool 4 and from tool 5 to tool 8, and the drilling force of tool 4

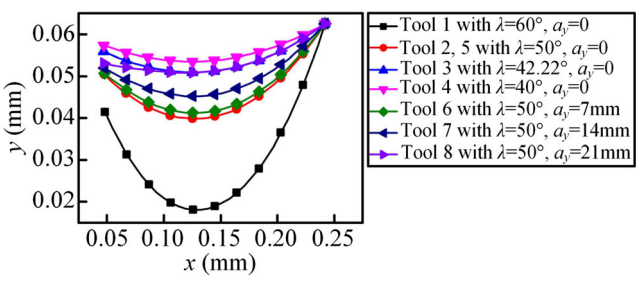

Fig. 21 The shape of the cutting lip

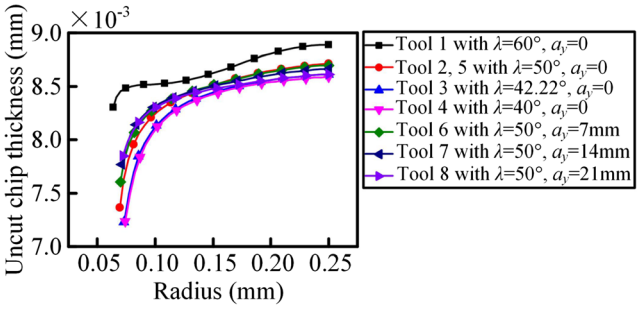

Fig. 22 The uncut chip thickness along the cutting lip

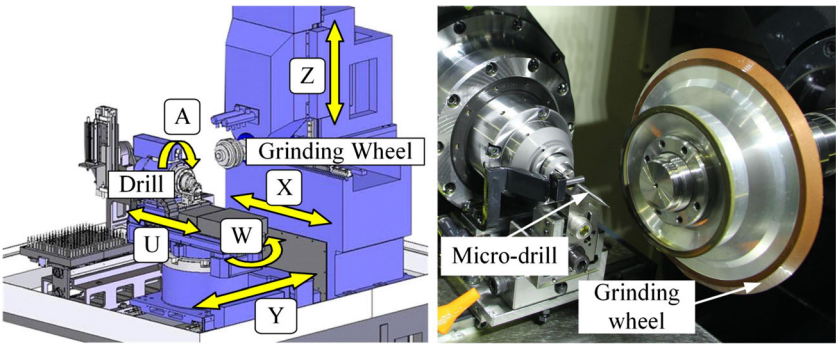

Fig. 23 The grinding experiment setup

with flute generated by smaller wheel installation angle is the smallest among the different micro-drills.

The flute profile has a great influence on the cutting lip shape, affects the rake angle, inclination angle, uncut chip thickness, and cut width, and finally affects the chip deformation and drilling force. The cutting lip shape and the corresponding uncut chip thickness a_c are shown in Figs. 21 and 22, and the calculation equation of the uncut chip thickness is expressed as [20]

$$\begin{aligned} a_c &= \frac{1}{2} f \cos\left(\sin^{-1}(\mathbf{k}\cdot\mathbf{r})\right)\cdot\sin\kappa_{re} \\ &= \frac{1}{2} f \cos\left(\sin^{-1}(\mathbf{k}\cdot\mathbf{r})\right)\cdot\sin\left(\cos^{-1}\left(\mathbf{o}\cdot\left(\frac{\mathbf{k}-(\mathbf{k}\cdot\mathbf{r})\mathbf{r}}{|\mathbf{k}-(\mathbf{k}\cdot\mathbf{r})\mathbf{r}|}\right)\right)\right), \mathbf{k} \\ &= (0,\ 0,\ 1) \end{aligned} \tag{13}$$

where **r** and **o** are the unit vectors normal to working reference plane and orthogonal plane.

It can be seen that the shape of the cutting lip becomes straighter from tool 1 to 4, which leads to the decrease of the uncut chip thickness and cut width. So, the shearing force and shear energy rate decrease. In addition, as discussed in Sect. 4.1, the slip length of the chip along the rake face and the convolution of the chip along the drill body reduces from tool 1 to tool 4, and this results in the reduction of the friction force and friction energy rate. So, the total cutting energy rate and cutting force decrease, and the tool force components, i.e., the thrust force and torque, become decreased from tool 1 to tool 4. Similarly, the drilling force decreases from tool 5 to tool 8 due to the decrease of shearing force and friction force. Moreover, for tools 3 and 8, the shapes of the cutting lips are basically coincident due to the same radial rake angle discussed in Sect. 3.1, so the drilling forces of tools 3 and 8 are almost equal, even though one is conventional flute profile and the other one is parabolic flute profile.

Therefore, for tool 4 with flute generated by smaller wheel installation angle, the cutting lip is straighter than other micro-drills, resulting in the smaller uncut chip thickness and cut width, so the workpiece material plastic deformation and shearing force by tool 4 are smaller. The spiral chip is generated during the drilling process, leading to the reduction of the friction force between the chip and drill rake face. So, the total cutting force and the tool force components, i.e., the thrust force and torque, by tool 4 are smaller than those of other micro-drills.

Furthermore, it should be pointed out that the radial rake angle of tool 4 is smaller than that of other micro-drills, and

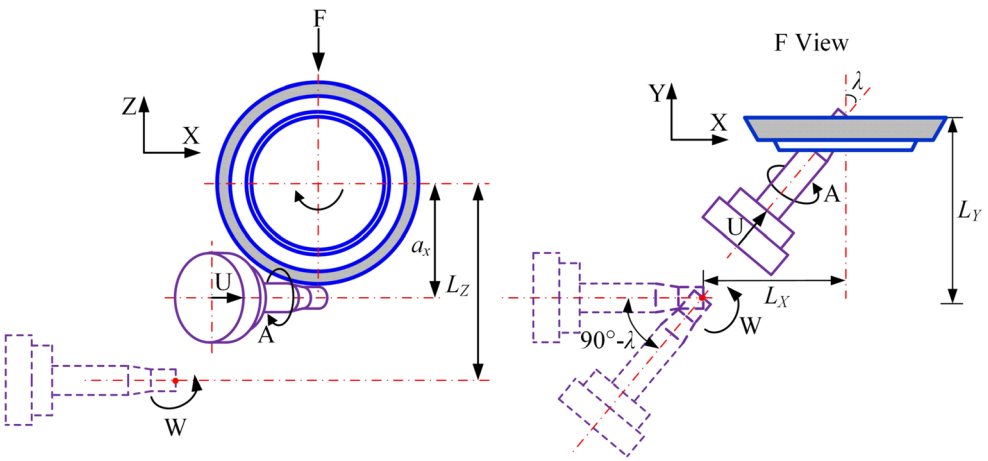

Fig. 24 Schematic illustration of the flute grinding process

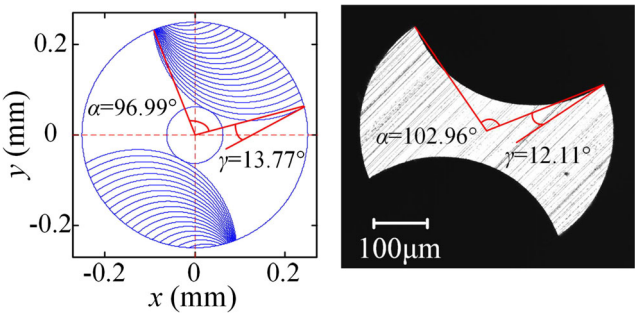

Fig. 25 The numerical simulation and grinding experiment result of the optimized drill flute

the drilling force should be larger in theory. But the simulation result of micro-drilling shows that the thrust force and torque by tool 4 are smaller than those of other micro-drills, due to the cutting lip shape, the uncut chip thickness and cut width, the chip deformation, and the chip morphology. Hence, the result illustrates that the radial rake angle cannot directly and effectively reflect the merits of the drilling performance, and the comprehensive analysis on the cutting process of micro-drills with different flute profiles is essential and significant.

5 Grinding experiments of the micro-drills

To verify the validity of the mathematical model of drill flute and the corresponding numerical simulation results, the optimized drill flute is fabricated using a six-axis CNC grinding machine (CNS7d, by Makino seiki Co., Ltd.). The configuration of the machine is shown in Fig. 23. During the grinding process, the drill shank is clamped to make the drill axis coincide with *A*-axis, and the drill can move along *U*-axis and *Y*-axis, rotate about *W*-axis, while the grinding wheel can move along *X*-axis and *Z*-axis.

The flute grinding process is shown in Fig. 24; L_X, L_Y, and L_Z are the distance between drill point and grinding wheel along *X*, *Y*, and *Z* axes in the initial position. Firstly, *W*-axis should rotate angle 90°-λ; the drill should move along *Y*-axis by $y_1 = L_Y$, while the grinding wheel moves along the *X*-axis and *Z*-axis by $x_1 = L_X + a_y / \cos\lambda$, $z_1 = L_Z - a_x$, where, $\lambda = 40°$, $a_x = 67.5625$ mm, and $a_y = 0$. Then, the flute is fabricated by the coordinated motion of *U*-axis and *A*-axis, i.e., *A*-axis rotates angle φ, while *U*-axis moves distance $r\varphi/\tan(\beta_0)$, where $r = 0.25$ mm, $\beta_0 = 30°$.

The ground drill flute profile and the corresponding numerical simulation result are shown in Fig. 25. The result shows that the practical result is in accordance with the theoretical result and verifies the validity of the mathematical model of drill flute and its numerical simulation result. At last, the optimized micro-drill is fabricated using the six-axis CNC grinding machine, and the grinding experiment result of micro-drill is shown in Fig. 26.

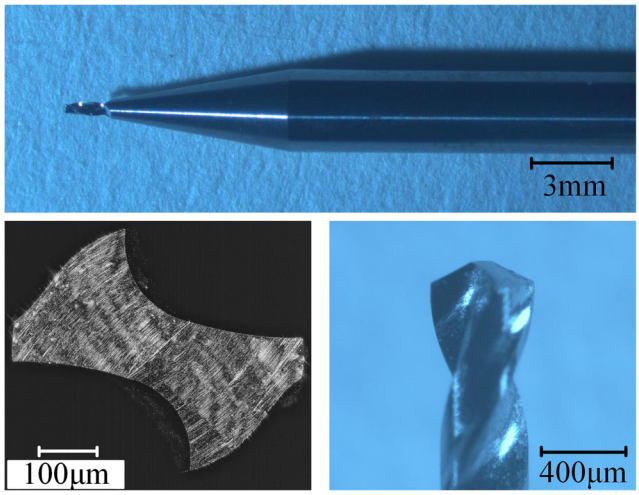

Fig. 26 The grinding experiment result of the optimized micro-drill

6 Conclusions

This paper presents a method for modeling and optimization of the micro-drill flute. Considering the wheel installation angle and the offset distance from wheel origin to the drill blank origin, the flute profile of micro-drill is simulated by MATLAB software firstly. Then based on the numerical simulation results, the 3D model of the micro-drill with different flute profiles is established by UG software. Finally, the micro-drilling process on 304 austenitic stainless steel is simulated by DEFORM software, and the chip morphology and drilling force are analyzed and discussed. Some conclusions can be summarized as follows:

1. The wheel installation angle has an obvious effect on the flute profile and its radial rake angle and flute width, and the wheel offset distance only influences the flute width evidently. The radial rake angle increases rapidly with the increased wheel installation angle and decreases slightly with the increased wheel offset distance. The flute width of drill flute increases obviously with the decreased wheel installation angle and the increased wheel offset distance.
2. Compared with other tools, micro-drill with flute ground by smaller wheel installation angle owns straighter cutting lip shape and larger chip evacuation capacity, and its thrust force and torque are smaller than those of other micro-drills due to the smaller uncut chip thickness and cut width. Moreover, spiral chip is generated caused by the intense side curl and up curl of the chip, resulting in the easiness of the chip removal.
3. The mathematical model of the drill flute and its numerical simulation result are validated by experimentally fabricating the micro-drill flute. At last, the optimized micro-drill is manufactured by a six-axis CNC grinding machine, and its flute profile is fabricated using a standard conical grinding wheel with a smaller wheel installation angle.

Acknowledgements This work was supported by National Natural Science Foundation of China (No. 51575049), National Basic Research Program of China (No. 2015CB059900), and Beijing Institute of Technology (BIT) Foundation for Fundamental Research (No. 20150342013).

References

1. Kang SK, Ehmann KF, Lin C (1996) A CAD approach to helical groove machining—I. Mathematical model and model solution. Int J Mach Tools Manuf 36(1):141–153
2. Hsieh JF (2006) Mathematical model and sensitivity analysis for helical groove machining. Int J Mach Tools Manuf 46(10):1087–1096
3. Kim JH, Park JW, Ko TJ (2008) End mill design and machining via cutting simulation. Comput Aided Des 40(3):324–333
4. Ehmann KF, DeVries MF (1990) Grinding wheel profile definition for the manufacture of drill flutes. CIRP Annals-Manufacturing Technology 39:153–156
5. Kang D, Armarego EJA (2003) Computer-aided geometrical analysis of the fluting operation for twist drill design and production. II. Backward analysis, wheel profile, and simulation studies. Mach Sci Technol 7:249–266
6. Ren BY, Tang YY, Chen CK (2001) The general geometrical models of the design and 2-axis NC machining of a helical end-mill with constant pitch. J Mater Process Technol 115:265–270
7. Chen WY, Chang PC, Liaw SD, Chen WF (2005) A study of design and manufacturing models for circular-arc ball-end milling cutters. J Mater Process Technol 161:467–477
8. Pham TT, Ko SL (2010a) A manufacturing model of an end mill using a five-axis CNC grinding machine. Int J Adv Manuf Technol 48:461–472
9. Pham TT, Ko SL (2010b) A practical approach for simulation and manufacturing of a ball-end mill using a 5-axis CNC grinding machine. J Mech Sci Technol 24(1):159–163
10. Zhang W, Wang XF, He FB, Xiong DL (2006) A practical method of modelling and simulation for drill fluting. Int J Mach Tools Manuf 46:667–672
11. Karpuschewski B, Jandecka K, Mourek D (2011) Automatic search for wheel position in flute grinding of cutting tools. CIRP Annals-Manufacturing Technology 60:347–350
12. Tang F, Bai J, Wang X (2014) Practical and reliable carbide drill grinding methods based on a five-axis CNC grinder. Int J Adv Manuf Technol 73:659–667
13. Ren L, Wang SL, Yi LL, Sun SL (2016) An accurate method for five-axis flute grinding in cylindrical end-mills using standard 1V1/1A1 grinding wheels. Precis Eng 43:387–394
14. Beju LD, Brîndaşu DP, Muţiu NC, Rothmund J (2015) Modeling, simulation and manufacturing of drill flutes. Int J Adv Manuf Technol 83:1–17
15. Kim YH, Ko SL (2002) Development of design and manufacturing technology for end mills in machining hardened steel. J Mater Process Technol 130:653–661
16. Xiao SL, Wang LM, Chen ZC, Wang SQ, Tan AM (2013) A new and accurate mathematical model for computer numerically controlled programming of 4Y1 wheels in 2½-axis flute grinding of cylindrical end-mills. J Manuf Sci Eng 135:041008
17. Zhang SY, Liang ZQ, Wang XB, Zhou TF, Jiao L, Yan P, Jian HC (2016) Grinding process of helical micro-drill using a six-axis CNC grinding machine and its fundamental drilling performance. Int J Adv Manuf Technol 86(9):2823–2835
18. Yan L, Jiang F (2013) A practical optimization design of helical geometry drill point and its grinding process. Int J Adv Manuf Technol 64(9):1387–1394
19. Kang SK (1993) Micro-drill geometry and grinding. PhD thesis. Northwestern University, USA
20. Wang J (1994) Development of new drilling force models for improving drill point geometries. University of Michigan, USA